Kunde Korinna, Gerda Lydia (Orcid ID: 0000-0002-1655-0088)

González-Santana David (Orcid ID: 0000-0001-8726-7768)

Tagliabue Alessandro (Orcid ID: 0000-0002-3572-3634)

Mahaffey Claire (Orcid ID: 0000-0002-4215-7271)

Lohan Maeve, C (Orcid ID: 0000-0002-5340-3108)

Iron Distribution in the Subtropical North Atlantic:

The Pivotal Role of Colloidal Iron

K. Kunde[1], N. J. Wyatt[1], D. González-Santana[1], A. Tagliabue[2], C. Mahaffey[2], M. C. Lohan[1]

[1] Ocean and Earth Sciences, University of Southampton, Waterfront Campus, National Oceanography Centre, European Way, Southampton, SO14 3ZH, United Kingdom

[2] Department of Earth, Ocean and Ecological Sciences, University of Liverpool, 4 Brownlow Street, Liverpool, Merseyside L69 3GP, United Kingdom

Corresponding author: Korinna Kunde (K.Kunde@soton.ac.uk)

Key Points

- Size-fractionation reveals that colloidal iron is more important than soluble iron for distribution of dissolved iron in North Atlantic

- Colloidal iron is the predominantly active species at key supply and removal processes of the dissolved iron cycle

- Global comparison suggests that the colloidal iron fraction in mesopelagic zone is determined by the local lithogenic contribution

Abstract

The low availability of the essential micronutrient iron (Fe) in the ocean impacts the efficiency of the biological carbon pump, and hence, it is vital to elucidate its sources, sinks and internal cycling. We present size-fractionated dissolved Fe (dFe, <0.2 μm) measurements from 130 surface samples and seven full-depth profiles from the subtropical North Atlantic during summer 2017, and demonstrate the pivotal role of colloidal (cFe, 0.02 to 0.2 μm) over soluble (sFe, <0.02 μm) Fe in controlling the dFe distribution. In the surface (<5 m), a strong west-to-east decrease in dFe (1.53 to 0.26 nM) was driven by a dust gradient which retained dFe predominantly as cFe (61 to 85 % of dFe), while sFe remained largely constant at 0.19±0.05 nM. In the euphotic zone, the attenuation of dFe resulted from the depletion of cFe (0 to 30 % of dFe), with scavenging as an important driver. In the mesopelagic, cFe was released from sinking biogenic and lithogenic particles, creating a zone of elevated dFe (0.7 to 1.0 nM) between 400 to 1100 m depth. While the ocean interior, below the mesopelagic and above the seafloor boundary, exhibited a narrow range of cFe (40 to 60 % of dFe), the abyssal cFe fraction varied in range from 25 to 75 % due to interactions with seafloor sediments and a hydrothermal source with almost 100 % cFe. Overall, our results produced an hourglass shape for the vertical cFe-to-dFe fraction, and highlight the primary control of cFe on the dFe distribution.

Plain Language Summary

Phytoplankton require nutrients such as phosphorus, nitrogen and iron. Of these, iron is particularly interesting due to the paradox of its requirement for life-supporting mechanisms on the one hand and its low oceanic concentrations on the other. Iron is >1000-fold lower than the "traditional" nutrients. Hence, it is important to know how much iron is introduced to the ocean (sources), how much is removed (sinks), and how it is processed during its

residence in the water. This study addressed these questions by measuring the iron concentrations in the subtropical North Atlantic. Our samples were filtered through two filter sizes to investigate the distributions of iron's different size fractions, a popular tool to gain a detailed understanding of the overall iron cycle. We found that the smallest size fraction, "soluble iron", does not vary much throughout the water column, but the slightly larger "colloidal iron" varies a lot, especially in the upper ocean and close to the seafloor, where dynamic supply and removal processes occur. The unequal behaviour of these fractions is an important finding that will improve the accuracy of biogeochemical models for iron, which in turn can improve the prediction of phytoplankton growth in the present and future ocean.

1 Introduction

Iron (Fe) is an essential micronutrient for marine primary production due to its enzymatic requirement in key metabolic functions such as photosynthesis, respiration and the acquisition of macronutrients (Falkowski, 1997; Morel, 2003). For example, diazotrophs require Fe to fix dinitrogen (N_2) into more bioavailable forms, where surface nitrate concentrations are sufficiently low to limit biological activity (<10 nM), such as in the oligotrophic North Atlantic gyre (Mahaffey et al., 2003; Moore et al., 2009). However, due to the low solubility of Fe(III), the thermodynamically stable Fe species in seawater (Kuma et al., 1996; Liu & Millero, 1999), chronically low surface water dissolved Fe (dFe) concentrations prevail (<0.1 nM) that limit phytoplankton growth in large regions and result in a less efficient biological carbon pump (Moore et al., 2013). Concentrations exceeding the solubility limit can be maintained by organic ligands, (Gledhill & Buck, 2012) which form a crucial component in the regulation of Fe bioavailability in the oceans (Tagliabue et al., 2014).

Superimposed on its low concentration is the "hybrid" nature of Fe, where it displays a combined nutrient-type and scavenged-type vertical distribution (Bruland & Lohan, 2004). Scavenging, an umbrella term for adsorption, absorption, aggregation processes and the eventual transfer to the particulate phase (Honeyman & Santschi, 1989; Wells & Goldberg, 1992), reduces the residence time of Fe and exacerbates the potential of Fe limitation.

Of the total Fe pool, only dissolved Fe (dFe), a continuum of exchangeable physicochemical species, is considered bioavailable (Tagliabue et al., 2017). Despite great progress in our understanding of the oceanic dFe cycle, thanks to GEOTRACES (http://www.geotraces.org/) and similar studies, major unknowns persist. These include its residence time with estimates ranging between 5 to 500 years (Tagliabue et al., 2016), and its bioavailability with variations over three orders of magnitude depending on the Fe-substrate (Lis et al., 2015). To determine the complex mechanisms controlling the particle reactivity and bioavailability of Fe, total Fe can be separated into different size classes using operationally defined filter sizes (Table 1). Size fractions of Fe can be defined as soluble (sFe<0.02 µm), colloidal (0.02 µm<cFe<0.2 µm), dissolved (dFe<0.2 µm), apparent particulate (pFe_{app}>0.2 µm) and total dissolvable (TDFe, unfiltered) Fe.

Soluble Fe represents the "truly dissolved" Fe fraction, although only a small portion is present as free Fe', while the majority is complexed by organic ligands such as high-affinity siderophores (Gledhill & Buck, 2012). Soluble Fe is highly bioavailable in both free and complexed forms and arguably the favourable species for biological uptake (Lis et al., 2015; Shaked et al., 2005). In contrast, cFe, present in suspended nanoparticles or bound to colloidal-sized organic ligands, is rarely or less readily bioavailable (Chen & Wang, 2001; Wang & Dei, 2003) but can constitute almost 100 % of dFe (Fitzsimmons, Carrasco, et al., 2015).

Colloids serve as conduit for transferring Fe between the soluble and particulate phases in a two-step scavenging process termed "Brownian pumping", which involves the sorption of sFe onto the colloidal intermediate followed by the aggregation of colloids to larger particles (Honeyman & Santschi, 1989; Wells & Goldberg, 1992). While scavenging and biological uptake result in the transfer from the dissolved to the particulate phase, particles simultaneously replenish the dFe inventory via dissolution or remineralisation (Milne et al., 2017).

Published data on size-fractionated Fe revealed two opposing hypotheses concerning the role of sFe and cFe in driving the Atlantic dFe distribution in particular. Largely invariable concentrations of sFe and variable cFe concentrations led Bergquist et al. (2007) to conclude that a dynamic colloidal phase controls the dFe distribution. In contrast, Fitzsimmons, Carrasco, et al. (2015) and Fitzsimmons and Boyle (2014) measured variability in both cFe and sFe, and hence attributed a joint control on dFe by both size fractions.

The North Atlantic is heavily impacted by Fe-rich dust deposition from the Sahara, and to lesser extent from Europe and North America, receiving >40 % of the global dust flux to the ocean (Jickells et al., 2005). Prevailing wind patterns further introduce seasonality to the dust deposition, with highest dust-derived Fe fluxes in the summer (Sedwick et al., 2005), while the seasonal migration of the Intertropical Convergence Zone controls wet deposition, which is efficient for delivering Fe to the ocean (Schlosser et al., 2014). Atmospheric deposition imprints elevated dFe concentrations in the surface waters (~0.5 to 1.0 nM) of the North Atlantic that are in excess of those observed in the less dusty South Atlantic (<0.5 nM) (Ussher et al., 2013). This strong external Fe source to the otherwise oligotrophic subtropical gyre, creates a unique biogeochemical setting with a hotspot for N_2 fixation (Moore et al., 2009). Hence, the North Atlantic is a key region for the understanding of the oceanic Fe cycle.

Using the physicochemical speciation of Fe from a 3,000 km-long surface transect and seven full-depth profiles (Fig. 1), the present study addresses the questions: 1) What external and internal factors drive the distribution of Fe in the subtropical North Atlantic? 2) How do sFe and cFe fractionally contribute to the dFe budget? 3) And which fraction exerts the greater regulatory control?

2 Materials and Methods

2.1 Sample Collection

Seawater samples were collected during cruise JC150 (Fig. 1) in the subtropical North Atlantic in summer (26th June to 12th August 2017), sampling between Guadeloupe and Tenerife on-board the *R.R.S. James Cook*. Seven stations were occupied for vertical profiling whilst underway surface sampling (~5 m) was conducted along the transect at a resolution of ~0.23 ° longitude. Seawater samples were collected using a titanium rosette fitted with 24x10 L trace metal-clean Teflon-coated OTE (Ocean Test Equipment) bottles and a CTD profiler (Sea-bird Scientific) deployed on a conducting Kevlar wire. Upon recovery, the OTE bottles were transported into a class-1000 clean air van and pressurized (0.7 bar) with compressed air filtered in-line through a 0.2 µm PTFE filter capsule (Millex-FG 50, Millipore). Sub-samples for dFe were filtered through 0.2 µm membrane cartridge filters (Sartobran-300, Sartorius) into trace metal-clean 125 ml low-density polyethylene (LDPE) bottles and acidified to pH 1.7 (0.024 M) by addition of 12 M ultrapure hydrochloric acid (HCl, Romil, UpA) under a class-100 laminar flow hood (Lohan et al., 2006). Samples for sFe went through an additional in-line filtration step inside a laminar flow hood through 0.02 µm syringe filters (Anotop, Whatman) before acidification. The filtration manifold consisted of PTFE manifold tubing and PVC peristaltic pump tubing, cleaned daily with weak 1 M HCl (SpA, Romil) and conditioned prior to use with low Fe seawater (Wu et al. 2001; Ussher et al. 2010). A new

filter was used for each sFe sample. Samples for TDFe were collected unfiltered and then acidified. For the underway samples, seawater was pumped into the trace metal clean van using a Teflon diaphragm pump (A-15, Almatec) connected by acid-washed PVC tubing to a towed "Fish"-sampler. These samples were filtered in-line (<0.2 μm,) and acidified, while the filtration step was omitted for TDFe and no underway sFe samples were taken.

2.2 Iron Measurements

All sFe, dFe and TDFe samples were analysed in triplicate (three analytical peaks) using flow injection analysis with chemiluminescence detection (Floor et al., 2015; Obata et al., 1997) inside a class-1000 clean air laboratory either on-board or at the National Oceanography Centre Southampton, UK. Briefly, each sample was spiked one hour prior to analysis with 0.013 M ultrapure H_2O_2 (Sigma-Aldrich) to ensure the complete oxidation of Fe(II) to Fe(III) (Lohan et al., 2006). Each sample was buffered in-line to pH 3.5 to 4.0 using a 0.15 M ammonium acetate (Romil, SpA) before Fe(III) was pre-concentrated onto the cation exchange resin Toyopearl-AF-Chelate 650 M (Tosohaas) typically for 60 s at a flow rate of 1.5 ml min^{-1}. Following a rinse step of a weak 0.013 M HCl (Romil, SpA), Fe was liberated from the resin using 0.24 M HCl (Romil, SpA) and entered the reaction stream where it mixed with a pre-cleaned 0.015 mM luminol solution containing 70 μl L^{-1} triethylenetetramine (Sigma-Aldrich), buffered to pH 9.4 to 9.6 using a 1 M ammonia solution (Romil, SpA). Chemiluminescence occurred following the addition of 0.4 M H_2O_2, with the light signal detected (425 nm) by a photomultiplier tube (H82259, Hamamatsu). Iron concentrations were quantified using standard additions (TraceCERT, Fluka Analytical) to low Fe seawater. The limit of detection (3x the standard deviation of the lowest addition) was 0.03±0.02 nM (n=59), whilst the precision of three analytical peaks was 2.78±2.02 % (n=1764). The procedural blank was assessed at the beginning of each analytical run using ultrahigh purity water, treated in the same way as the samples, and averaged 0.05±0.03 nM

(n=69). Accuracy was established by repeat quantification of dFe in the SAFe reference samples yielding 0.11±0.02 nM (n=6) and 0.94±0.04 nM (n=17) for SAFe S and SAFe D2 respectively, which agree with the reported consensus values (S=0.095±0.008 nM; D2=0.96±0.02 nM).

2.3 Auxiliary Parameters

Samples for chlorophyll-*a* (Chl-*a*) analysis from both the OTE bottles and the underway system were filtered through 0.7 µm glass microfiber filters (Whatman GF/F) and extracted in 90 % acetone overnight (Holm-Hansen et al., 1965). The Chl-*a* extract was measured on a pre-calibrated (Spinach Chl-*a* Standard, Sigma) fluorimeter (Turner Designs Trilogy) and used to calibrate the fluorescence sensor on the CTD (Seabird 911+) daily. Salinity was calibrated on-board using an Autosal 8400B salinometer (Guildline). Dissolved oxygen (O_2) was measured by a Seabird SBE43 sensor, calibrated on-board using a photometric automated Winkler titration system (Carritt & Carpenter, 1966). Turbidity was monitored using a WETLabs BBRTD light scattering sensor.

2.4 Calculations and Definitions

Mixed layers were calculated using a density change of 0.03 kg m^{-3} (de Boyer Montégut et al., 2004). To integrate Fe budgets across the upper ocean (Section 3.2.1), the 1026.5 kg m^{-3} isopycnal was chosen as lower boundary. We did not try to capture a specific water mass, instead the intention was to compare the total Fe inventory in this layer across stations. This resulted in integration depths between 350 m at Station 1 and 220 m at Station 7. Shallower isopycnals would not have captured the full DCM at Station 7 (Fig. 6). Similarly, for remineralisation effects on dFe budgets in the mesopelagic (Section 3.2.3), we chose the isopycnals 1026.30 and 1027.50 kg m^{-3} as boundaries because they cover the oxycline from ~180 to 130 µmol kg^{-1} between 220 to 1000 m depth (Fig. S2). Apparent oxygen utilisation

(AOU) was used to calculate dFe:C ratios (AOU:C=1.6, Martin et al., 1989). For a global comparison of size-fractionated dFe distributions in the mesopelagic (Section 3.2.3) we included all cFe measurements from the referenced datasets that lie within 10 % of the maximum AOU at each station. For consistency, we used the AOU from the global annual 1° grid of the World Ocean Atlas 2018 (Garcia et al., 2013). Extracted AOU values were in excellent agreement with those calculated from measured O_2 concentrations during JC150. Stations reportedly influenced by sedimentary or hydrothermal input were excluded. Annual dust fluxes were extracted from Albani et al. (2016). Colloidal Fe data was binned by annual dust flux in 1 g m^{-2} yr^{-1} increments.

3 Results and Discussion

3.1 Large-scale Distribution of Dissolved Iron

Figure 2 displays the full water column distribution of dFe across the transect with four main features of note: 1) an enrichment in the immediate surface layer, 2) a subsurface minimum between 50 to 200 m, 3) an increase in dFe in the mesopelagic between 400 to 1100 m, and 4) a large point-source in the deep ocean at 45 °W (Fig. 2). The most eye-catching of these features was the mid-section hotspot with up to 27 nM at 3300 m at Station 4, attributed to hydrothermal input from the Snakepit vent field on the mid-Atlantic Ridge. The surface enrichment was most pronounced west of 54 °W with ≥1 nM dFe at Stations 1 and 2 (Fig. 3), likely as a result of Fe-rich dust deposition from North Africa. In contrast, distinct dFe minima were present in the subsurface at all stations across the gyre with concentrations as low as 0.09 nM at 60 m in the east (Station 7). Concurrent with the location of the deep chlorophyll-*a* maxima (DCM), these dFe minima probably result from the combination of scavenging and biological uptake. Below the DCM to a depth of ~1200 m, dFe gradually increased to maxima of 0.7 to 1.0 nM, with highest concentrations in the east. Mesopelagic

dFe enrichments correlated with AOU (R^2=0.58, n=100) and probably derived from the continued dissolution of sinking dust particles and from the remineralisation of organic matter. Away from external sources and from the influence of biological processes, the concentration of dFe in the ocean interior below the low O_2 waters and above the seafloor water-sediment interface was 0.67±0.14 nM, excluding the hydrothermal influence observed at Station 4.

Overall, we show that dust acted as the main driver of the surface Fe distribution with far-reaching effects on the underlying water column, while sediment resuspension and hydrothermalism were important in the abyss. Scavenging was the major sink. Our main finding is that the cFe distribution results in an "hourglass" pattern with depth. This is due to the decoupling of cFe and sFe, where the major sources and sinks of dFe result in increases or decreases of the cFe budget, with large ranges in both the surface ocean and close to the seafloor.

The current understanding of the partitioning between cFe and sFe for regulating the dFe distribution stems from the pioneering work done by Bergquist et al. (2007) and more recently by Fitzsimmons, Carrasco, et al. (2015), the latter of which, indicated an equal control between cFe and sFe, given the evidence for a more dynamic soluble phase compared to Bergquist et al.'s (2007) conclusions that colloids alone accounted for the observed partitioning. Based on our colloidal Fe data, we argue it is a balance of both of these mechanisms depending on the presence or absence of external drivers at different depths. Where dFe is supplied or removed, the colloidal and soluble phases were strongly decoupled with cFe taking on the greater regulatory control for the dFe distribution and shaping the wide top and bottom sections of the hourglass. In the interior ocean away from external sources or sinks, the dFe partitioning was balanced between cFe and sFe in a steady-state equilibrium, which formed the neck of the hourglass.

3.2 Distribution of Soluble and Colloidal Iron

3.2.1 The Dusty Surface Ocean

The JC150 transect underlies the northern extent of the Saharan dust plume that provides approximately 200 Tg yr^{-1} of dust to the North Atlantic (Jickells et al., 2005). Dust deposition from Sahara-influenced air masses regulates the Fe budget in the surface North Atlantic via aerosol solubilisation (Sedwick et al., 2005; Ussher et al., 2013) and is overwhelmingly the largest flux of Fe to this region (Ussher et al., 2013).

Our surface sampling revealed a longitudinal decrease of surface dFe concentrations from west to east, with a maximum of 1.53 nM at 60 °W and a minimum of 0.26 nM at 31 °W (Fig. 3). Concentrations >0.5 nM are typical for the dust-dominated North Atlantic (Fitzsimmons, Carrasco, et al., 2015; Hatta et al., 2015; Measures et al., 2008; Sedwick et al., 2005), which contrast with concentrations of <0.25 nM for the dust-limited South Atlantic, Pacific and Southern Ocean (Buck et al., 2017; Chever et al., 2010; Fitzsimmons, Hayes, et al., 2015; Nishioka et al., 2001). The west-east gradient we observed appeared counter-intuitive with regard to the location of the Saharan source. However, it was consistent with a compilation of upper ocean dFe data from the North Atlantic (Fig. 4), where Fe profiles appeared more influenced by dust in the west compared to the east. This is because large amounts of dust are entrained into the warm Saharan Air Layer (SAL), which is trapped at altitudes above the dust-free northeasterly trade wind inversion and exported westwards with the strong circulation of the Azores-Bermuda High during summer (Schepanski et al., 2009; Tsamalis et al., 2013). As the SAL descends westwards, the dust increasingly mixes into the marine boundary layer where it seeds the surface ocean (Tsamalis et al., 2013), thereby imprinting the longitudinal gradient of dust-derived Fe that we observe. Previous investigations into atmospherically-derived Fe at the Bermuda Atlantic Time-series Study

confirm a large Saharan dust source during summer (Fishwick et al., 2014; Sedwick et al., 2005).

Accompanying measurements of TDFe displayed a similar trend to dFe, decreasing from >3 nM in the west to <1 nM in the east, but with larger variability than dFe (Fig. 3). The dFe:pFe$_{app}$ ratio was 0.57±0.25 for the entire transect except for the most western sample at 60 °W. Here, the pFe$_{app}$ concentration was only 0.53 nM and the dFe concentration was 1.53 nM, resulting in a dFe:pFe$_{app}$ ratio of 2.87 in stark contrast to the remaining transect and suggests a lower influence of dust deposition at this location. The surface samples west of 58 °W (Station 1) were collected at lower latitudes (17.5 to 21.6 °N) than the remaining transect (≥22 °N) (Fig. 1), where the lower salinities (34 to 36) (Fig. 3) indicate the northern boundary of the seasonal Amazon and Orinoco River plumes (Fournier et al., 2015). Rijkenberg et al. (2014) showed a strong linear inverse correlation between dFe and salinity during summer 2013. Hence, the elevated dFe concentrations in the surface samples approaching Station 1 possibly originated from the river plume which may have lost pFe$_{app}$ relative to dFe during the seaward transport and mixing with seawater.

The concentrations of sFe from the shallowest depth from the CTD averaged 0.19±0.05 nM across the transect. Importantly, they displayed no west-to-east gradient, in contrast to the basin-scale distributions of the other Fe size fractions, and appeared to be independent of the magnitude of dFe and pFe$_{app}$ inputs. The average excludes the slightly elevated sFe concentration of 0.33 nM at 58 °W (Station 1), which was possibly an artefact of the Amazon and Orinoco River plumes.

What processes might be responsible for such small variation in the surface sFe concentrations? Potential biogeochemical controls include Fe-binding ligand distributions, a threshold for dust-derived Fe dissolution into the soluble phase, or a dilution threshold

beyond which sFe is unreactive. The two size-fractionated ligand studies available concluded that ligand distributions cannot account for size-fractionated Fe distributions alone (Cullen et al., 2006; Fitzsimmons, Bundy, et al., 2015). Moreover, surface sFe concentrations higher (Ussher et al., 2013) or lower (Chever et al., 2010) than our ~0.2 nM have been observed previously and render the threshold arguments unlikely. Alternatively, the resolution of our surface sFe data alongside the small variations in the concentrations may prevent the identification of a potential gradient for sFe and its biogeochemical controls.

Regardless, the subtlety of the changes in surface sFe concentrations implies that cFe was the driver of the gradient in dFe concentrations in surface waters across the subtropical North Atlantic. The colloidal contributions to the dFe pool were highest where dFe and TDFe concentrations were elevated as a result of dust input (and riverine input at Station 1), with values of 61 to 85 % cFe for dFe concentrations of 0.53 to 1.25 nM between Stations 1 and 6. The maximum colloidal contribution of 85 % cFe for a dFe concentration of 0.77 nM was observed at Station 3. In contrast, only 32 % of dFe was in the colloidal form at Station 7 where the dFe concentration was lowest (0.27 nM). While the high surface cFe fractions of >60 % were consistent with previous studies in the dust-dominated North Atlantic (Fitzsimmons, Carrasco, et al., 2015; Fitzsimmons & Boyle, 2014; Sedwick et al., 2005; Ussher et al., 2010), the absence of a surface colloidal maximum at Station 7 is rather atypical of observations from the North Atlantic and resembled the dust-limited surface waters of the Pacific (Fitzsimmons, Hayes, et al., 2015; Nishioka et al., 2001). The tight coupling of TDFe, dFe and cFe trends across the basin suggests that higher Fe in the particulate phase results in more dFe via cFe, and hence particles have an important influence on the dFe size partitioning. These links were similarly evident in the size-fractionated Fe datasets when plotting the top 50 m of the US-GEOTRACES GA03 section, just north of our

transect (Fitzsimmons, Carrasco, et al., 2015; Lam, 2018; Schlitzer et al., 2018; Twining, 2014).

Seawater leaches of aerosol particles showed that dust-derived dFe is predominantly retained as cFe in the ocean, either as eroded fragments or due to the authigenic formation of colloidal-sized Fe-oxyhydroxides or organic complexes (Fishwick et al., 2014), which explains the observed colloidal maxima in the high dFe-surface waters. Dust deposition is at its minimum in the eastern subtropical North Atlantic during summer because of the high-altitude transport of the SAL and the resulting deposition in the west. Hence, the unusually low colloidal fraction at Station 7 likely resulted from sampling this seasonal extreme. This is an important insight because the North Atlantic is often characterised in bulk as a high dust and high Fe region (Moore et al., 2009) but our results demonstrate the sensitivity of the Fe inventory to strong regional and seasonal variability within the subtropical North Atlantic. This sensitivity resulted in two endmembers along our section: A high dust endmember with a high colloidal contribution to dFe and a low dust endmember with a low colloidal contribution to dFe.

While the instantaneous effect of dust deposition in the immediate surface is on cFe, a dust-driven effect for sFe is apparent when considering the entire upper water column (using integrated Fe inventories). Increasing the sampling resolution enables us to detect impacts on the surface water column after the dust-derived Fe had the chance to undergo internal cycling. Dissolved Fe, cFe and pFe_{app} inventories were higher in the west than in the east, following a similar gradual longitudinal decrease as in the immediate surface (Fig. 3) confirming that dust affects the underlying layers too. Surprisingly, the sFe budget also decreased clearly from west to east, a trend not apparent in the immediate surface (Fig. 3). An important caveat is that the shoaling of the isopycnals towards the west lowers the integrated budgets. However, depth-normalised integrated Fe budgets portray the same overall

longitudinal trends for all size fractions. A possible mechanism driving the higher sFe in the upper ocean in the west versus the east is the indirect source from dust, by which Fe is partially mobilised from the colloidal into the soluble phase via ligands as suggested by aerosol leaching experiments (Fishwick et al., 2014). This transformation could increase the bioavailable portion of dFe.

3.2.2 Iron Depletion through the Euphotic Zone

Deep chlorophyll maxima (DCM) are a widespread phenomenon in the subsurface of the (sub)tropical oceans and positioned across the nutriclines, where macronutrient supply from deeper waters sustains low light-adapted primary production (Cullen, 2015). The upper water column distributions of macronutrients and Fe are decoupled due to greater remineralisation length scale of Fe (Boyd et al., 2017). Consequently, the DCM can become Fe-limited (Sunda & Huntsman, 1997). At most of our stations, the dFe concentration gradually decreased through the euphotic zone towards the DCM, often reaching minima between 60 to 200 m, where Chl-*a* peaked (Fig. 6a-g). Moreover, there was a gradual transition from the strongly dust-driven dFe profile at Stations 1 and 2, where the difference between surface maxima and DCM minima were largest, to the more nutrient-like profile at Station 7 (Fig. 6a-g). These two endmembers resulted from the dust-driven surface dFe distribution (Fig. 3) and appear to be characteristic of the western and eastern North Atlantic, respectively (Fig. 4).

The attenuation of the dFe signal between the surface and the DCM was clearly controlled by the attenuation of cFe, which typically decreased to <30 % of dFe in the DCM (Fig. 6a-g) or even disappeared completely, which was most pronounced at Station 5. Concentrations of sFe were less variable between surface and DCM with slight increases observed in the centre (Station 5) or on the slopes (Stations 2 and 4) of the DCM, where it accounted for up to 100 % of dFe. These characteristics are in line with previous observations from the DCM of the

Atlantic (Fitzsimmons, Carrasco, et al., 2015) and Pacific (Fitzsimmons, Hayes, et al., 2015). In other words, cFe was removed over sFe in the euphotic zone despite the widespread understanding that sFe is more bioavailable (Birchill et al., 2017). This leads to the question: Does the gradual depletion of dFe via cFe through the euphotic zone mark a biological preference for cFe over sFe or does scavenging control the observed Fe distribution?

It is possible that the elevated Fe demands of the DCM community (Hogle et al., 2018; Sunda & Huntsman, 1997) force the utilisation of the cFe pool, e.g. via a ligand-mediated transfer into the soluble phase prior to uptake (Chen & Wang, 2001; Wang & Dei, 2003). If the uptake is time-lagged from the transfer between phases, cFe would be depleted and (ligand-bound) sFe would accumulate, which matches the observations in many of our depth profiles. However, the few size-fractionated ligand studies concluded that ligand distributions alone cannot account for the observed Fe distributions (Cullen et al., 2006; Fitzsimmons, Bundy, et al., 2015), while Fitzsimmons, Bundy, et al. (2015) found no increase in soluble-sized ligand production in the DCM. In addition, cFe and Chl-*a* were not strongly negatively correlated (R^2=-0.27, surface to 1026.5 kg m^{-3}), which would reflect biological uptake, and we did not observe an enrichment in pFe$_{app}$, which would capture the cellular Fe pool.

Instead, we observed simultaneous minima of pFe$_{app}$ and cFe in the DCM (Fig. 6h and Fig. S1) and a stronger positive correlation of cFe with turbidity as an indicator of particle abundance (R^2=0.48). This strengthens the argument that cFe is not simply transferred from the dissolved to the particulate phase but both phases are removed together, leading us (and others: Ohnemus & Lam, 2015) to conclude that dFe (in form of cFe) is shuttled out of euphotic zone via sinking particles and that this scavenging is a principal mechanism driving the distributions of cFe, dFe and pFe$_{app}$ here. Biological uptake appears to be a minor contributor to the removal of dFe (cFe) but may be important in maintaining sFe levels via the replenishment from other Fe fractions.

Despite the likely co-occurrence of these different processes, our size-fractionated measurements identified the preferential removal of cFe, not sFe, alongside pFe_{app} and hence, the potential importance of particle scavenging over biological uptake for the removal of Fe. The increasing resolution of size-fractionated Fe measurements repeatedly confirm the cFe minima in the DCM as an intriguing phenomenon of the subtropical ocean which warrants further investigations, as highlighted in a recent review by Anderson (2020), because the central implication of these minima is that despite large Fe-rich dust depositions, the efficient removal of dFe leads to a potential Fe-limitation in the DCM.

3.2.3 The Mesopelagic – Mirroring the Surface Ocean

It is a longstanding paradigm that the distributions of major nutrients below the euphotic zone are shaped by the balance between a preformed and a regenerated component, which are the result of physical transport and the microbial degradation of organic matter (remineralisation) respectively. Nutrients released by remineralisation can sustain a major fraction of primary production when re-supplied into the surface. Unlike the macronutrients, Fe is subjected to additional processes, such as scavenging, that affect its subsurface inventory (Hatta et al., 2015; Tagliabue et al., 2014; Twining et al., 2015). AOU provides a measure of remineralisation at depth, which is the result of local remineralisation that acts on sinking biogenic particles and of the transport of aging water masses. We observed a zone of lower O_2 concentrations (120 to 150 µM) and elevated dFe concentrations (0.7 to 1.0 nM) between 400 to 1100 m depth (Fig. 2 and Fig. S2). The dFe:C ratio along the oxycline was 5.8±0.50 µmol mol^{-1} (R^2=0.58, n=100), which was within the range of ratios previously reported for the North Atlantic (Fitzsimmons, Carrasco, et al., 2015; Hatta et al., 2015; Milne et al., 2017) but lower than cellular ratios in phytoplankton of 33 to 57 µmol mol^{-1} (Twining et al., 2015), which demonstrates the impact of scavenging as a post-remineralisation sink. Microbial

recycling also occurs throughout the upper ocean, but O_2 concentrations are in equilibrium with the atmosphere and hence AOU cannot function as a measure of remineralisation.

In contrast to the biogenic-dominated macronutrients, the majority of Fe-bearing particles in our study region are lithogenic. Boyd et al. (2010) showed that the dissolution of Fe from lithogenic particles dominates over the release from biogenic material in the North Atlantic. Furthermore, Fe isotope measurements revealed that the entire water column may be impacted by dust (Conway & John, 2014). If the mesopelagic dFe inventory is driven by the release from lithogenic particles, it leads to the hypothesis that the dominance of cFe over sFe may be observed at depth because dust-derived Fe occurs predominantly as cFe. Within our sample subset around the AOU maximum, the dFe size partitioning was 37±16 % cFe, but a global comparison of published size-fractionated dFe data from the mesopelagic, enables us to probe this theory (Fig. 7). Regions of high annual dust flux (6.2 to 22.6 g m^{-2} yr^{-1}) display higher mean cFe contributions of 60 and 48 % of dFe, respectively. In contrast, regions of lower dust flux (1.0 to 5.1 g m^{-2} yr^{-1}) exhibit lower mean cFe contributions of 39 to 42 % of dFe. At dust fluxes of <0.3 g m^{-2} yr^{-1} the cFe contributions are lowest with 35 % of dFe. This pattern of high colloidal fractions in the mesopelagic at high dust in contrast to low colloidal fractions at low dust is analogous to the surface ocean, where colloidal maxima are present in regions of high dust (this study; Fitzsimmons, Carrasco, et al., 2015) and absent in dust-limited regions (Nishioka et al., 2001). The reason colloidal fractions from high-dust regions are not as high in the mesopelagic compared to the surface (61 to 85 %) may be explained by the two-step model of Fishwick et al. (2014), in which some cFe is transferred into the soluble phase over time. Furthermore, a portion of the released cFe is likely re-scavenged.

The tug-of-war between these mechanisms is eventually manifested in the 37±16 % cFe that we observed.

The main result of this global comparison is a strong coupling between the speciation of dFe in the mesopelagic and the surface dust deposition. The implication is that the spatial variability of subsurface dFe distributions is driven by regional dust flux. This highlights the sensitivity of the Fe cycle to changes in atmospheric supply, especially in the light of past and future changes. Therefore, constraining the mesopelagic Fe cycling as a major pathway for the re-supply to the surface requires the investigation of cFe specifically rather than bulk dFe.

3.2.4 The Deep Iron Inventory – Hydrothermalism and Seafloor-Sediment Interactions

While atmospheric deposition provides the largest input of Fe to the surface North Atlantic, modelling efforts showed that sedimentary release and hydrothermal venting prevail globally by at least one order of magnitude (Tagliabue et al., 2010, 2014). The JC150 transect captured the influence of both of these sources on the deep Fe inventory.

Station 4 targeted the Snakepit hydrothermal vent field located around 3500 m on the mid-Atlantic ridge (Beaulieu, 2015). Anomalies in the turbidity confirm that we sampled the neutrally buoyant hydrothermal plume with a dFe concentration maximum of 27 nM at 3300 m (Fig. 8). Hydrothermally-derived Fe can overcome near-field precipitation and be transported over large distances (>1000 km) (Resing et al., 2015; Saito et al., 2013) via its stabilisation either by organic complexes (Sander & Koschinsky, 2011) or in colloidal-sized nanoparticles (Revels et al., 2015; Yücel et al., 2011). Our plume dFe samples were composed of 92±3 % (n=4) cFe, similar to the 89 to 96 % cFe in the plume of the nearby Trans-Atlantic Geotraverse vent field (Fitzsimmons, Carrasco, et al., 2015).

Apart from its role as an important source of Fe, the mid-Atlantic ridge also acts as a physical barrier between the eastern and western abysses. The physical speciation measurements of Fe

revealed opposing trends on either side of the ridge. In the west, we observed elevated pFe_{app}

concentrations of 6.4 nM at 5400 m at Station 1 and 4.0 nM at 5900 m at Station 2, compared

to ≤2.0 nM for all other stations (data not shown). No equivalent increase in dFe

concentrations was observed (Fig. 2) and the two deepest samples collected at 50 and 20 m

above the seafloor decreased by 0.13 and 0.09 nM at Station 1 and 2, respectively. The cFe

contributed only 26 and 29 % to the dFe budget, lower than values from the overlying water

column. In the east, this pattern was reversed. At Station 5, dFe concentrations reached 1.26

nM at 20 m above the seafloor with a cFe fraction of 76 %, and at Station 7, 63 % of dFe was

in the colloidal form although no simultaneous increase in the dFe concentration was

detected. Gardner et al. (2017) showed that thick benthic nepheloid layers form in the western

North Atlantic and Lam et al. (2015) and Revels et al. (2015) reported higher lithogenic and

Fe-rich particle abundances in this area, which is evident in our pFe_{app} measurements. The

large surface area and high concentration of the resuspended particles hold high scavenging

potential, so that the scavenging of dFe in the form of cFe onto sedimentary particles may

dominate over dissolution and produce a cFe signature of <50 % alongside decreased dFe

concentrations. In contrast, dissolution dominates over scavenging in the east, which drives

cFe contributions >50 % and increase the dFe inventory.

The background dFe concentration in the ocean interior (>1027.50 kg m^{-3} and above ocean-

sediment interface) away from any external or internal sources or sinks was 0.67±0.14 nM,

excluding the hydrothermal Station 4. Slightly higher dFe concentrations were observed in

the interior of the western basin compared to the eastern basin (Fig. 2), which appears to be a

persistent feature in the North Atlantic (Fitzsimmons, Carrasco, et al., 2015; Hatta et al.,

2015) and may be the result of different water masses and currents on either side of the ridge.

Our Station 6 crossed over with Station USGT11-20 of the US-GEOTRACES section GA03

(Boyle et al., 2015) showing close agreement (Fig. S3), and demonstrate the relatively

constant dFe distribution in the deep ocean. Dissolved Fe in the ocean interior was partitioned into 49±14 % cFe, in agreement with the previously reported 50:50 % partitioning for this region (Fitzsimmons, Carrasco, et al., 2015). This balanced distribution of cFe and sFe was proposed to result from a steady-state equilibrium between cFe and sFe (Fitzsimmons, Carrasco, et al., 2015) and our results are in line with this hypothesis.

4 Synthesis – The Colloidal Hourglass

We quantified the partitioning of dFe into soluble and colloidal phases in the subtropical North Atlantic to address the underlying questions regarding how sFe and cFe contribute to and regulate the dFe distribution. We found that the cFe contribution to the dFe pool produced an hourglass shape against depth that arises from the dominant variability of cFe over sFe (Fig. 9). Our results show that cFe is the main source of dFe to the water column via the dissolution of particles, and also the main sink via scavenging. In other words, whenever dFe is introduced or removed, it is the cFe that is driving these changes. This result reinforces the idea that cFe holds a pivotal role in the oceanic Fe cycle and that it may be a crucial component for improving Fe models.

The dynamic upper ocean encompasses a range of sources and sinks that led to a large range of colloidal fractions between the surface and ~1200 m (0 to 86 % of dFe) (Fig. 9). In the near surface, elevated cFe contributions of 61 to 85 % coincident with high dFe concentrations were the result of dust supply. Throughout the euphotic zone, cFe decreased to 0 to 30 % through its preferential scavenging onto sinking particles. Loss of cFe to the sFe phase and subsequent biological uptake further contributed to the removal of cFe in the DCM. Our hourglass figure highlights that on a small vertical scale (from surface to DCM), the change in dFe (cFe) is large, especially where the surface maximum is strong and the implication is that despite large surface inputs Fe-limitation in the DCM is possible. In the

dust-loaded subtropical North Atlantic, the vast majority of the sinking particles are lithogenic, and dominate the release of Fe over biogenic particles even at depths of remineralisation (Boyd et al., 2010). Here, we observed a tug-of-war between the continued leaching of Fe from lithogenics that increases cFe, and competing mechanisms that act to remove cFe efficiently. This balance resulted in a colloidal contribution of 37±16 % of dFe that we observed. These competing mechanisms include the immediate re-scavenging and aggregation of released cFe associated with particles (both lithogenic and biogenic) and the disaggregation of cFe into sFe. A global comparison showed that the lithogenic nature of dust particles determines the cFe fraction in the mesopelagic, with lower dust fluxes resulting in lower colloidal fractions and vice versa.

At the ocean-seafloor boundary, cFe ranged widely from 26 to 76 % of dFe (Fig. 9). We observed a west-to-east difference with the lower cFe contributions in the west (26 to 47 %) and the higher cFe contributions in the east (52 to 75 %), due to regional differences in benthic nepheloid layers.

The narrow range of colloidal fractions in the ocean interior formed the neck of the hourglass, where the partitioning into sFe and cFe falls into a balanced distribution of 1:1 (49±14 % cFe of dFe), as the result of a steady-state exchange between the fractions. The near-vent hydrothermal signal of almost 100 % cFe is a clear exception.

Our study indicates that cFe predominantly drives the overall surface-to-seafloor dFe distribution in the subtropical North Atlantic. Colloidal Fe and dFe are reasonably well correlated ($R^2_{cFe:dFe}$=0.61, n=95), while the correlation between sFe and dFe is weak ($R^2_{sFe:dFe}$=0.14, n=95), excluding hydrothermal samples. In the ocean interior, our data is consistent with Fitzsimmons, Carrasco et al.'s (2015) model where dFe partitions equally into sFe and cFe (~40 to 60 %). An important caveat is that the resolution of our measurements is

lower than Fitzsimmons, Carrasco et al.'s (2015), and the concentrations of the different Fe fractions fall into a narrower range in our dataset. Regardless, a similar "colloidal hourglass" shape is observed with the larger dataset by Fitzsimmons, Carrasco, et al. (2015) (Fig. S4).

5 Conclusions

Despite the dramatic increase of oceanic dFe measurements in the past decade, biogeochemical models struggle to constrain fundamental parameters of the Fe cycle such as scavenging rates and residence times. The physicochemical speciation of Fe is less well resolved than the bulk dissolved phase, but it bears the potential to illuminate some of these uncertainties. Our dataset of size-fractionated Fe from the subtropical North Atlantic demonstrates the pivotal role of cFe, the larger-sized species in the dFe continuum, for controlling the distribution of dFe. We found that cFe is the predominantly active species in key supply and removal processes of dFe compared with the smaller sFe which showed a more constant behaviour. Moreover, a global compilation of colloidal data allowed us to detect a sensitive dust-driven linkage between surface and mesopelagic dFe inventories which would have been concealed by making dissolved measurements only. Currently, the important role of cFe is not represented in models. Hence, advancing our understanding of the oceanic Fe cycle demands the extension of size-fractionated measurements at a global scale and the incorporation of an explicit cFe term in models.

Acknowledgments and Data

Author contributions

References

Albani, S., Mahowald, N. M., Murphy, L. N., Raiswell, R., Moore, J. K., Anderson, R. F., et al. (2016). Paleodust variability since the Last Glacial Maximum and implications for iron inputs to the ocean. *Geophysical Research Letters*, *43*(8), 3944–3954. https://doi.org/10.1002/2016gl067911

Anderson, R. F. (2020). GEOTRACES: Accelerating Research on the Marine Biogeochemical Cycles of Trace Elements and Their Isotopes. *Annual Review of Marine Science*, *12*(9), 9.1-9.37. https://doi.org/10.2138/gselements.14.6.377

Beaulieu, S. E. (2015). InterRidge Global Database of Active Submarine Hydrothermal Vent Fields: prepared for InterRidge, Version 3.3. Retrieved from http://vents-data.interridge.org

Bergquist, B. A., Wu, J., & Boyle, E. A. (2007). Variability in oceanic dissolved iron is dominated by the colloidal fraction. *Geochimica et Cosmochimica Acta*, *71*(12), 2960–2974. https://doi.org/10.1016/j.gca.2007.03.013

Birchill, A. J., Milne, A., S. Woodward, E. M., Harris, C., Annett, A., Rusiecka, D., et al. (2017). Seasonal iron depletion in temperate shelf seas. *Geophysical Research Letters*, *44*(3), 8987–8996. https://doi.org/10.1002/2017GL073881

Boyd, P. W., Ibisanmi, E., Sander, S. G., Hunter, K. A., & Jackson, G. A. (2010). Remineralization of upper ocean particles: Implications for iron biogeochemistry. *Limnology and Oceanography*, *55*(3), 1271–1288. https://doi.org/10.4319/lo.2010.55.3.1271

Boyd, Philip W., Ellwood, M. J., Tagliabue, A., & Twining, B. S. (2017). Biotic and abiotic retention, recycling and remineralization of metals in the ocean. *Nature Geoscience*, *10*(3), 167–173. https://doi.org/10.1038/ngeo2876

de Boyer Montégut, C., Madec, G., Fischer, A. S., Lazar, A., & Iudicone, D. (2004). Mixed layer depth over the global ocean: An examination of profile data and a profile-based climatology. *Journal of Geophysical Research C: Oceans*, *109*(12), 1–20. https://doi.org/10.1029/2004JC002378

Boyle, E. A., Anderson, R. F., Cutter, G. a., Fine, R., Jenkins, W. J., & Saito, M. A. (2015). Introduction to the U.S. GEOTRACES North Atlantic Transect (GA-03): USGT10 and

USGT11 cruises. *Deep Sea Research Part II*, *116*, 1–5. https://doi.org/10.1016/j.dsr2.2015.02.031

Bruland, K. W., & Lohan, M. C. (2004). The control of trace metals in seawater. In J. P. Riley & R. Chester (Eds.), *Chemical Oceanography* (2nd ed., Vol. 6, pp. 157–220). New York: Academic Press.

Buck, K. N., Sedwick, P. N., Sohst, B., & Carlson, C. A. (2017). Organic complexation of iron in the eastern tropical South Pacific: Results from US GEOTRACES Eastern Pacific Zonal Transect (GEOTRACES cruise GP16). *Marine Chemistry*, *201*, 229–241. https://doi.org/10.1016/j.marchem.2017.11.007

Carritt, D. E., & Carpenter, J. H. (1966). Comparison and Evaluation of Currently Employed Modifications of the Winkler Method for Determining Dissolved Oxygen in Seawater; a NASCO Report. *Journal of Marine Research*, *24*, 286–318.

Chen, M., & Wang, W. (2001). Bioavailability of natural colloid-bound iron to marine plankton : Influences of colloidal size and aging. *Limnology and Oceanography*, *46*(8), 1956–1967. https://doi.org/10.4319/lo.2001.46.8.1956

Chever, F., Bucciarelli, E., Sarthou, G., Speich, S., Arhan, M., Penven, P., & Tagliabue, A. (2010). Physical speciation of iron in the Atlantic sector of the Southern Ocean along a transect from the subtropical domain to the Weddell Sea Gyre. *Journal of Geophysical Research: Oceans*, *115*(10), 1–15. https://doi.org/10.1029/2009JC005880

Conway, T. M., & John, S. G. (2014). Quantification of dissolved iron sources to the North Atlantic Ocean. *Nature*, *511*(7508), 212–215. https://doi.org/10.1038/nature13482

Cullen, J., Bergquist, B., & Moffett, J. W. (2006). Thermodynamic characterization of the partitioning of iron between soluble and colloidal species in the Atlantic Ocean. *Marine Chemistry*, *98*(2–4), 295–303. https://doi.org/10.1016/J.MARCHEM.2005.10.007

Cullen, J. J. (2015). Subsurface Chlorophyll Maximum Layers: Enduring Enigma or Mystery Solved? *Annual Review of Marine Science*, *7*(1), 207–239. https://doi.org/10.1146/annurev-marine-010213-135111

Falkowski, P. G. (1997). Evolution of the nitrogen cycle and its influence on the biological sequestration of CO2 in the ocean. *Nature*, *387*(6630), 272–275. https://doi.org/10.1038/387272a0

Fishwick, M. P., Sedwick, P. N., Lohan, M. C., Worsfold, P. J., Buck, K. N., Church, T. M., & Ussher, S. J. (2014). The impact of changing surface ocean conditions on the dissolution of aerosol iron. *Global Biogeochemical Cycles*, *28*, 1235–1250. https://doi.org/10.1002/2014GB004921

Fitzsimmons, J. N., & Boyle, E. A. (2014). Both soluble and colloidal iron phases control dissolved iron variability in the tropical North Atlantic Ocean. *Geochimica et Cosmochimica Acta*, *125*, 539–550. https://doi.org/10.1016/j.gca.2013.10.032

Fitzsimmons, J. N., Hayes, C. T., Al-Subiai, S. N., Zhang, R., Morton, P. L., Weisend, R. E., et al. (2015). Daily to decadal variability of size-fractionated iron and iron-binding ligands at the Hawaii Ocean Time-series Station ALOHA. *Geochimica et Cosmochimica Acta*, *171*, 303–324. https://doi.org/10.1016/j.gca.2015.08.012

Fitzsimmons, J. N., Carrasco, G. G., Wu, J., Roshan, S., Hatta, M., Measures, C. I., et al. (2015). Partitioning of dissolved iron and iron isotopes into soluble and colloidal phases

along the GA03 GEOTRACES North Atlantic Transect. *Deep-Sea Research Part II: Topical Studies in Oceanography*, *116*, 130–151. https://doi.org/10.1016/j.dsr2.2014.11.014

Fitzsimmons, J. N., Bundy, R. M., Al-Subiai, S. N., Barbeau, K. A., & Boyle, E. A. (2015). The composition of dissolved iron in the dusty surface ocean: An exploration using size-fractionated iron-binding ligands. *Marine Chemistry*, *173*, 125–135. https://doi.org/10.1016/j.marchem.2014.09.002

Floor, G. H., Clough, R., Lohan, M. C., Ussher, S. J., Worsfold, P. J., & Quetel, C. R. (2015). Combined uncertainty estimation for the determination of the dissolved iron amount content in seawater using flow injection with chemiluminescence detection. *Limnology and Oceanography: Methods*, *13*(12), 673–686. https://doi.org/10.1002/lom3.10057

Fournier, S., Chapron, B., Salisbury, J., Vandemark, D., & Reul, N. (2015). Comparison of spaceborne measurements of sea surface salinity and colored detrital matter in the Amazon plume. *Journal of Geophysical Research: Oceans*, *120*, 3177–3192. https://doi.org/10.1002/2014JC010441.Received

Garcia, H. E., Locarnini, R. A., Boyer, T. P., Antonov, J. I., Mishonov, A. V., Baranova, O. K., et al. (2013). World Ocean Atlast 2013: Vol. 3: Dissolved Oxygen, Apparent Oxygen Utilization, and Oxygen Saturation. In S. Levitus & A. V. Mishonov (Eds.), *NOAA Atlas NESDIS 75* (p. 27 pp.).

Gardner, W. D., Tucholke, B. E., Richardson, M. J., & Biscaye, P. E. (2017). Benthic storms, nepheloid layers, and linkage with upper ocean dynamics in the western North Atlantic. *Marine Geology*, *385*, 304–327. https://doi.org/10.1016/j.margeo.2016.12.012

Gledhill, M., & Buck, K. N. (2012). The organic complexation of iron in the marine environment: A review. *Frontiers in Microbiology*, *3*, 1–17. https://doi.org/10.3389/fmicb.2012.00069

Hatta, M., Measures, C. I., Wu, J., Roshan, S., Fitzsimmons, J. N., Sedwick, P., & Morton, P. (2015). An overview of dissolved Fe and Mn distributions during the 2010–2011 U.S. GEOTRACES north Atlantic cruises: GEOTRACES GA03. *Deep Sea Research Part II: Topical Studies in Oceanography*, *116*, 117–129. https://doi.org/10.1016/j.dsr2.2014.07.005

Hogle, S. L., Dupont, C. L., Hopkinson, B. M., King, A. L., Buck, K. N., Roe, K. L., et al. (2018). Pervasive iron limitation at subsurface chlorophyll maxima of the California Current. *Proceedings of the National Academy of Sciences of the United States of America*, *115*(52), 13300–13305. https://doi.org/10.1073/pnas.1813192115

Holm-Hansen, O., Lorenzen, C. J., Holmes, R. W., & Strickland, J. D. (1965). Fluorometric Determination of Chlorophyll. *ICES Journal of Marine Science*, *30*(1), 3–15.

Honeyman, B. D., & Santschi, P. H. (1989). A Brownian-pumping model for oceanic trace metal scavenging: Evidence from Th isotopes. *Journal of Marine Research*, *47*(4), 951–992. https://doi.org/10.1357/002224089785076091

Jickells, T. D., An, Z. S., Andersen, K. K., Baker, A. R., Bergametti, C., Brooks, N., et al. (2005). Global iron connections between desert dust, ocean biogeochemistry, and climate. *Science*, *308*(5718), 67–71. https://doi.org/10.1126/science.1105959

Kuma, K., Nishioka, J., & Matsunaga, K. (1996). Controls on iron(III) hydroxide solubility in

seawater: The influence of pH and natural organic chelators. *Limnology and Oceanography*, *41*(3), 396–407. https://doi.org/10.4319/lo.1996.41.3.0396

Lam, P. J. (2018). Size-fractionated major and minor particle composition and concentration from R/V Knorr KN199-04, KN204-01 in the subtropical North Atlantic Ocean from 2010-2011 (U.S. GEOTRACES NAT project). Biological and Chemical Oceanography Data Management Office (BCO-DMO). Retrieved from http://lod.bco-dmo.org/id/dataset/3871

Lam, P. J., Ohnemus, D. C., & Auro, M. E. (2015). Size-fractionated major particle composition and concentrations from the US GEOTRACES North Atlantic Zonal Transect. *Deep-Sea Research Part II: Topical Studies in Oceanography*, *116*, 303–320. https://doi.org/10.1016/j.dsr2.2014.11.020

Lis, H., Shaked, Y., Kranzler, C., Keren, N., & Morel, F. M. M. (2015). Iron bioavailability to phytoplankton: an empirical approach. *The ISME Journal*, *9*, 1003–1013. https://doi.org/10.1038/ismej.2014.199

Liu, X., & Millero, F. J. (1999). The solubility of iron hydroxide in sodium chloride solutions. *Geochimica et Cosmochimica Acta*, *63*(19–20), 3487–3497. https://doi.org/10.1016/S0016-7037(99)00270-7

Lohan, M. C., Aguilar-Islas, A. M., & Bruland, K. W. (2006). Direct determination of iron in acidified (pH 1.7) seawater samples by flow injection analysis with catalytic spectrophotometric detection: Application and intercomparison. *Limnology and Oceanography: Methods*, *4*, 164–171. https://doi.org/10.4319/lom.2006.4.164

Mahaffey, C., Williams, R. G., Wolff, G. A., Mahowald, N., Anderson, W., & Woodward, M. (2003). Biogeochemical signatures of nitrogen fixation in the eastern North Atlantic. *Geophysical Research Letters*, *30*(6), 33–36. https://doi.org/10.1029/2002GL016542

Martin, J. H., Gordon, R. M., Fitzwater, S., & Broenkow, W. W. (1989). Vertex: phytoplankton/iron studies in the Gulf of Alaska. *Deep Sea Research Part A, Oceanographic Research Papers*, *36*(5), 649–680. https://doi.org/10.1016/0198-0149(89)90144-1

Measures, C. I., Landing, W. M., Brown, M. T., & Buck, C. S. (2008). High-resolution Al and Fe data from the Atlantic Ocean CLIVAR-CO2 Repeat Hydrography A16N transect: Extensive linkages between atmospheric dust and upper ocean geochemistry. *Global Biogeochemical Cycles*, *22*(1), 1–10. https://doi.org/10.1029/2007GB003042

Milne, A., Schlosser, C., Wake, B. D., Achterberg, E. P., Chance, R., Baker, A. R., et al. (2017). Particulate phases are key in controlling dissolved iron concentrations in the (sub)tropical North Atlantic. *Geophysical Research Letters*, *44*(5), 2377–2387. https://doi.org/10.1002/2016GL072314

Moore, C. M., Mills, M. M., Achterberg, E. P., Geider, R. J., LaRoche, J., Lucas, M. I., et al. (2009). Large-scale distribution of Atlantic nitrogen fixation controlled by iron availability. *Nature Geoscience*, *2*(12), 867–871. https://doi.org/10.1038/ngeo667

Moore, C. M., Mills, M. M., Arrigo, K. R., Berman-Frank, I., Bopp, L., Boyd, P. W., et al. (2013). Processes and patterns of oceanic nutrient limitation. *Nature Geoscience*, *6*, 701–710. https://doi.org/10.1038/NGEO1765

Morel, F. M. M. (2003). The Biogeochemical Cycles of Trace Metals in the Oceans. *Science*,

300(5621), 944–947. https://doi.org/10.1126/science.1083545

Nishioka, J., Takeda, S., Wong, C. S., & Johnson, W. K. (2001). Size-fractionated iron concentrations in the northeast Pacific Ocean: Distribution of soluble and small colloidal iron. *Marine Chemistry*, *74*(2–3), 157–179. https://doi.org/10.1016/S0304-4203(01)00013-5

Obata, H., Karatani, H., Matsui, M., & Nakayama, E. (1997). Fundamental studies for chemical speciation of iron in seawater with an improved analytical method. *Marine Chemistry*, *56*(1–2), 97–106. https://doi.org/10.1016/S0304-4203(96)00082-5

Ohnemus, D. C., & Lam, P. J. (2015). Cycling of lithogenic marine particles in the US GEOTRACES North Atlantic transect. *Deep-Sea Research Part II: Topical Studies in Oceanography*, *116*, 283–302. https://doi.org/10.1016/j.dsr2.2014.11.019

Resing, J. A., Sedwick, P. N., German, C. R., & Jenkins, W. J. (2015). Basin-scale transport of hydrothermal dissolved metals across the South Pacific Ocean. *Nature*, *523*(7559), 200–203. https://doi.org/10.1038/nature14577

Revels, B. N., Ohnemus, D. C., Lam, P. J., Conway, T. M., & John, S. G. (2015). The isotopic signature and distribution of particulate iron in the North Atlantic Ocean. *Deep-Sea Research Part II: Topical Studies in Oceanography*, *116*, 321–331. https://doi.org/10.1016/j.dsr2.2014.12.004

Rijkenberg, M. J. A., Middag, R., Laan, P., Gerringa, L. J. A., van Aken, H. M., Schoemann, V., et al. (2014). The Distribution of Dissolved Iron in the West Atlantic Ocean. *PLoS ONE*, *9*(6), e101323. https://doi.org/10.1371/journal.pone.0101323

Saito, M. A., Noble, A. E., Tagliabue, A., Goepfert, T. J., Lamborg, C. H., & Jenkins, W. J. (2013). Slow-spreading submarine ridges in the South Atlantic as a significant oceanic iron source. *Nature Geoscience*, *6*(9), 775–779. https://doi.org/10.1038/ngeo1893

Sander, S. G., & Koschinsky, A. (2011). Metal flux from hydrothermal vents increased by organic complexation. *Nature Geoscience*, *4*(3), 145–150. https://doi.org/10.1038/ngeo1088

Schepanski, K., Tegen, I., & Macke, A. (2009). Saharan dust transport and deposition towards the tropicalnorthern Atlantic. *Atmospheric Chemistry and Physics*, *9*(4), 1173–1189. https://doi.org/10.5194/acp-9-1173-2009

Schlitzer, R., Anderson, R. F., Dodas, E. M., Lohan, M., Geibert, W., Tagliabue, A., et al. (2018). The GEOTRACES Intermediate Data Product 2017. *Chemical Geology*. https://doi.org/10.1016/j.chemgeo.2018.05.040

Schlosser, C., Klar, J. K., Wake, B. D., Snow, J. T., Honey, D. J., Woodward, E. M. S., et al. (2014). Seasonal ITCZ migration dynamically controls the location of the (sub)tropical Atlantic biogeochemical divide. *Proceedings of the National Academy of Sciences of the United States of America*, *111*(4), 1438–42. https://doi.org/10.1073/pnas.1318670111

Sedwick, P. N., Church, T. M., Bowie, A. R., Marsay, C. M., Ussher, S. J., Achilles, K. M., et al. (2005). Iron in the Sargasso Sea (Bermuda Atlantic Time-series Study region) during summer: Eolian imprint, spatiotemporal variability, and ecological implications. *Global Biogeochemical Cycles*, *19*(4). https://doi.org/10.1029/2004GB002445

Shaked, Y., Kustka, A. B., & Morel, F. M. M. (2005). A general kinetic model for iron acquisition by eukaryotic phytoplankton. *Limnology and Oceanography*, *50*(3), 872–

882. https://doi.org/10.4319/lo.2005.50.3.0872

Sunda, W. G., & Huntsman, S. A. (1997). Interrelated influence of iron , light and cell size on marine phytoplankton growth light and cell size on marine phytoplankton growth. *Nature*, *390*, 389–392. https://doi.org/10.1038/37093

Tagliabue, A., Bopp, L., Dutay, J.-C., Bowie, A. R., Chever, F., Jean-Baptiste, P., et al. (2010). Hydrothermal contribution to the oceanic dissolved iron inventory. *Nature Geoscience*, *3*(4), 252. https://doi.org/10.1038/ngeo818

Tagliabue, A., Mtshali, T., Aumont, O., Bowie, A. R., Klunder, M. B., Roychoudhury, A. N., & Swart, S. (2012). A global compilation of dissolved iron measurements: Focus on distributions and processes in the Southern Ocean. *Biogeosciences*, *9*(6), 2333–2349. https://doi.org/10.5194/bg-9-2333-2012

Tagliabue, A., Williams, R. G., Rogan, N., Achterberg, E. P., & Boyd, P. W. (2014). A ventilation-based framework to explain the regeneration-scavenging balance of iron in the ocean. *Geophysical Research Letters*, *41*, 7227–7236. https://doi.org/10.1002/2014GL061066.Received

Tagliabue, A., Aumont, O., & Bopp, L. (2014). The impact of different external sources of iron on the global carbon cycle. *Geophysical Research Letters*, *41*, 920–926. https://doi.org/10.1002/2013GL059059

Tagliabue, A., Aumont, O., DeAth, R., Dunne, J. P., Dutkiewicz, S., Galbraith, E., et al. (2016). How well do global ocean biogeochemistry models simulate dissolved iron distributions? *Global Biogeochemical Cycles*, *30*(2), 149–174. https://doi.org/10.1002/2015GB005289

Tagliabue, A., Bowie, A. R., Philip, W., Buck, K. N., Johnson, K. S., & Saito, M. A. (2017). The integral role of iron in ocean biogeochemistry. *Nature*, *543*(7643), 51–59. https://doi.org/10.1038/nature21058

Tsamalis, C., Chédin, A., Pelon, J., & Capelle, V. (2013). The seasonal vertical distribution of the saharan air layer and its modulation by the wind. *Atmospheric Chemistry and Physics*, *13*(22), 11235–11257. https://doi.org/10.5194/acp-13-11235-2013

Twining, B. S. (2014). Trace element concentrations in particles from R/V Knorr KN199-04, KN204-01 in the subtropical North Atlantic Ocean from 2010-2011 (U.S. GEOTRACES NAT project). Biological and Chemical Oceanography Data Management Office (BCO-DMO). Retrieved from http://lod.bco-dmo.org/id/dataset/3841

Twining, Benjamin S., Rauschenberg, S., Morton, P. L., & Vogt, S. (2015). Metal contents of phytoplankton and labile particulate material in the North Atlantic Ocean. *Progress in Oceanography*, *137*, 261–283. https://doi.org/10.1016/j.pocean.2015.07.001

Ussher, S. J., Achterberg, E. P., Sarthou, G., Laan, P., de Baar, H. J. W., & Worsfold, P. J. (2010). Distribution of size fractionated dissolved iron in the Canary Basin. *Marine Environmental Research*, *70*(1), 46–55. https://doi.org/10.1016/J.MARENVRES.2010.03.001

Ussher, S. J., Achterberg, E. P., Powell, C., Baker, A. R., Jickells, T. D., Torres, R., & Worsfold, P. J. (2013). Impact of atmospheric deposition on the contrasting iron biogeochemistry of the North and South Atlantic Ocean. *Global Biogeochemical Cycles*, *27*(4), 1096–1107. https://doi.org/10.1002/gbc.20056

Wang, W. X., & Dei, R. C. H. (2003). Bioavailability of iron complexed with organic colloids to the cyanobacteria Synechococcus and Trichodesmium. *Aquatic Microbial Ecology*, *33*(3), 247–259. https://doi.org/10.3354/ame033247

Wells, M. L., & Goldberg, E. D. (1992). Marine submicron particles. *Marine Chemistry*, *40*(1–2), 5–18. https://doi.org/10.1016/0304-4203(92)90045-C

Yücel, M., Gartman, A., Chan, C. S., & Luther, G. W. (2011). Hydrothermal vents as a kinetically stable source of iron-sulphide-bearing nanoparticles to the ocean. *Nature Geoscience*, *4*(6), 367–371. https://doi.org/10.1038/ngeo1148

Table 1 *The different size-fractionated Fe species used in this study. FIA-CL refers to flow injection analysis with chemiluminescence (see methods).*

Iron Species	Abbreviation	Filtration Size	Measurement
Soluble Fe	sFe	< 0.02 μm	Direct measurement by FIA-CL
Colloidal Fe	cFe	0.2 μm < cFe < 0.02 μm	Calculated using cFe = dFe - sFe
Dissolved Fe	dFe	< 0.2 μm	Direct measurement by FIA-CL
Apparent particulate Fe	pFe$_{app}$	> 0.2 μm	Calculated using pFe$_{app}$ = TDFe - dFe
Total dissolvable Fe	TDFe	Unfiltered	Direct measurement by FIA-CL
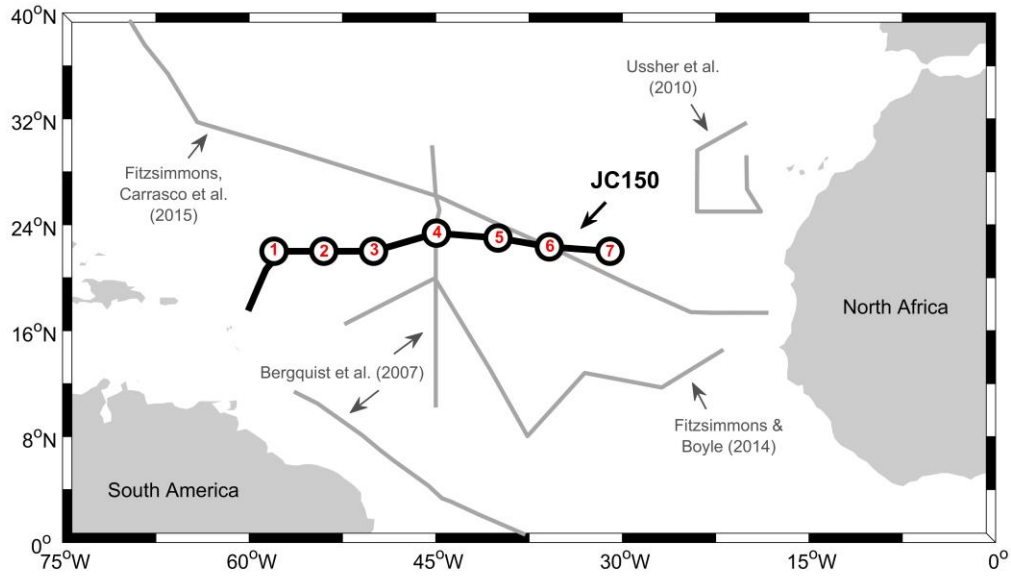
Figure 1 *Map of the North Atlantic Ocean. Indicated are the stations (black dots, red numbers) of full-depth sampling and the cruise track along which surface samples were taken (black line). Cruise tracks of previous studies on size-fractionated Fe in this region are also shown (grey lines, arrows pointing to associated publication).*
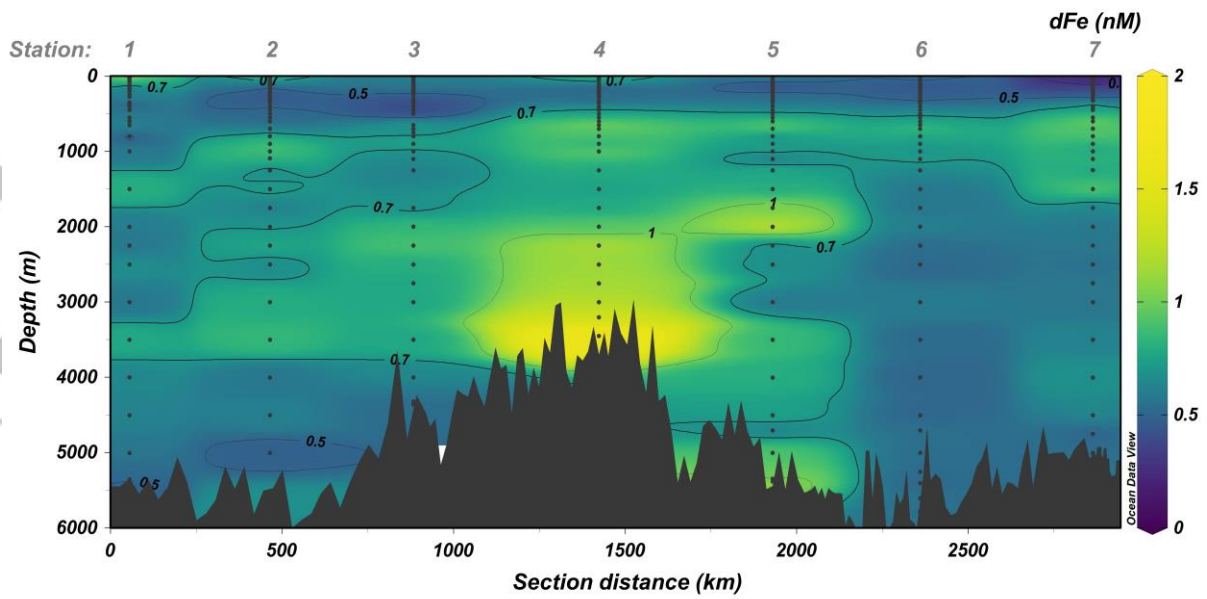
Figure 2 *Section plot of dFe concentrations against distance from West to East. The very high concentrations measured over the mid-oceanic ridge at Station 4 reach up to 27 nM, but are excluded from the colour bar. The plot was produced with Ocean Data View (Schlitzer, 2016), using weighted-average gridding for interpolation with maximum scale lengths of 35 and 33 ‰ for the x- and y-axes, respectively.*
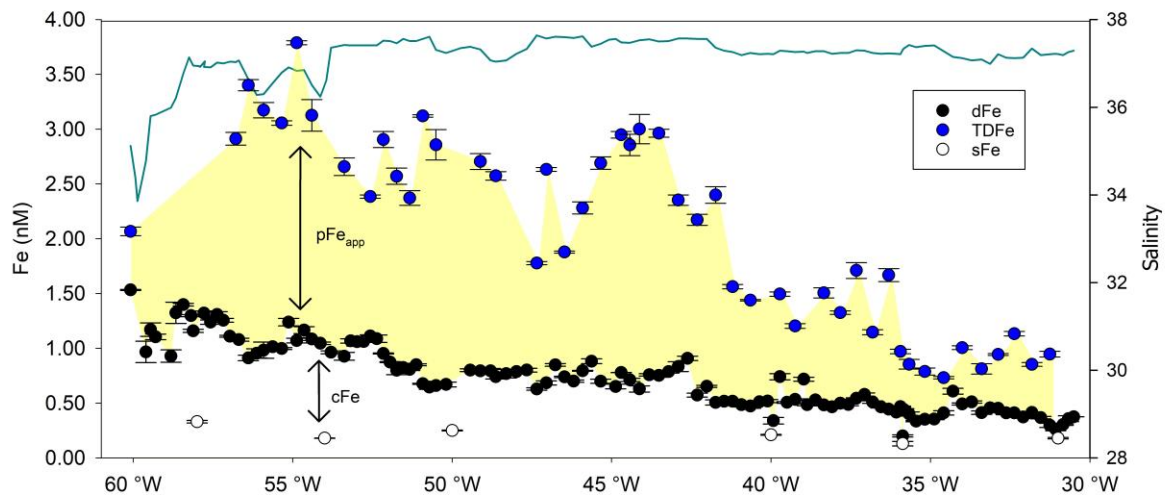
Figure 3 *Surface concentrations of dFe (black), sFe (white), TDFe (blue) and salinity (cyan line) against longitude along the cruise track. The calculated concentrations of cFe and pFe$_{app}$ are indicated with arrows. The dFe and TDFe concentrations are from the underway samples (~5 m), the sFe concentrations are from the shallowest water column samples (between 15 to 25 m) at each station. Error bars show one standard deviation of the mean concentration of three analytical replicates.*
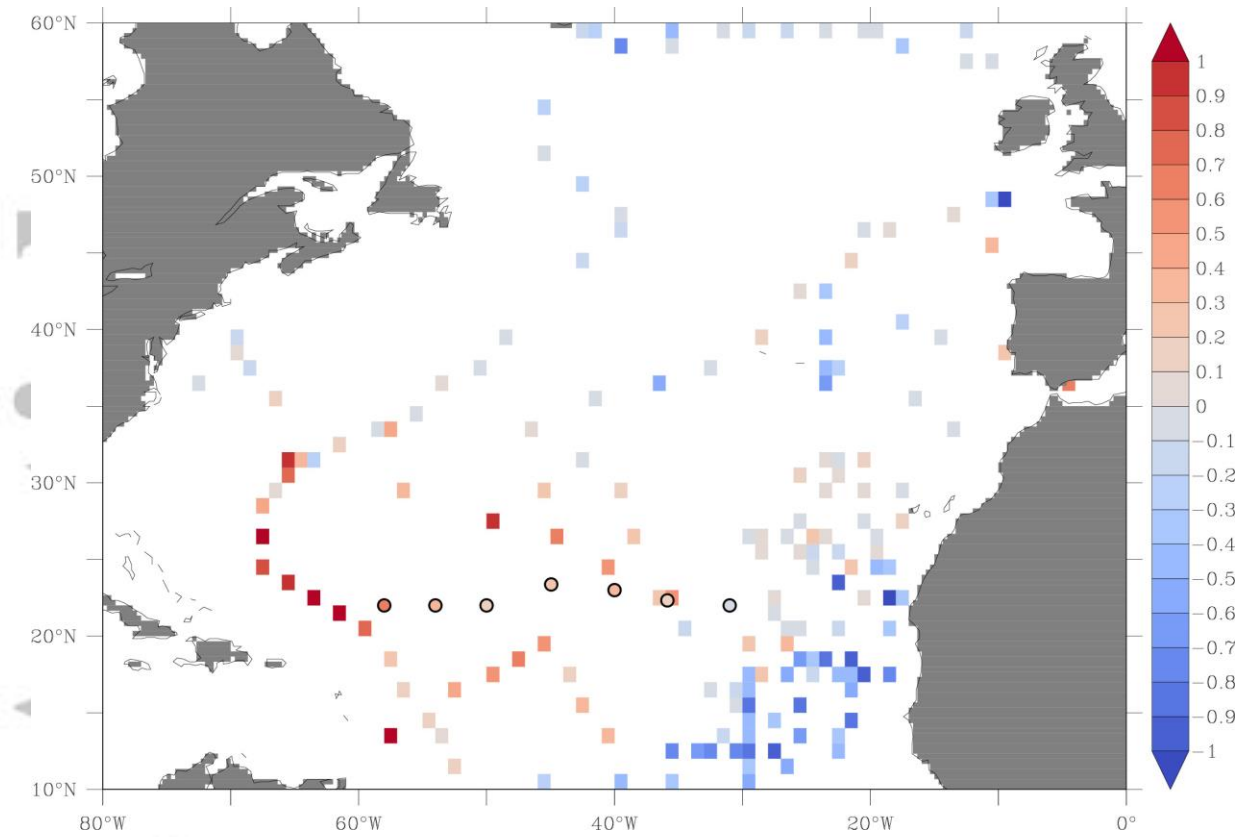
Figure 4 *Surface plot of the North Atlantic showing the difference of dFe concentration averaged over 0 to 50 m depth minus the concentration averaged over 100 to 150 m depth in a 1x1° grid. Red values show higher concentrations in surface than at depth, a typical dust-driven behaviour. Blue values shower lower concentrations in surface than at depth, a typical nutrient-like behaviour. Circles indicate JC150 stations. Data from Tagliabue et al. (2012) and augmented with data from the GEOTRACES Intermediate Data Product 2017 (Schlitzer et al., 2018).*
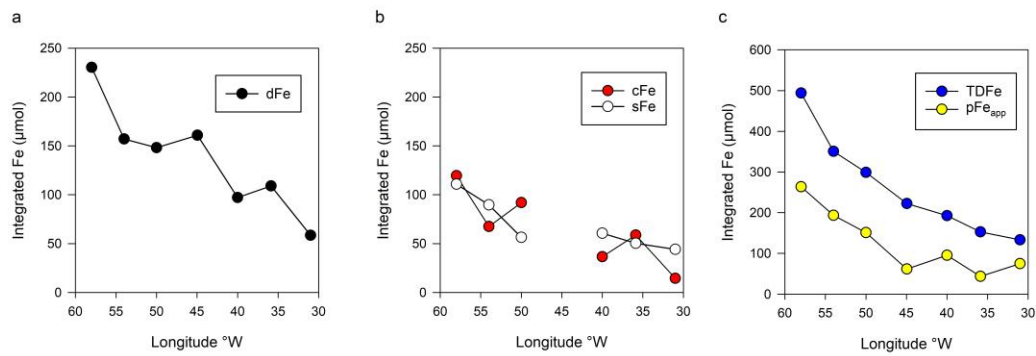
Figure 5 *The integrated upper ocean Fe inventories of **a)** dFe (black), **b)** sFe (white) and cFe (red), and **c)** TDFe (blue) and pFe$_{app}$ (yellow). Station 4 at 45 °W has been excluded for sFe and cFe due to the lack of data points.*
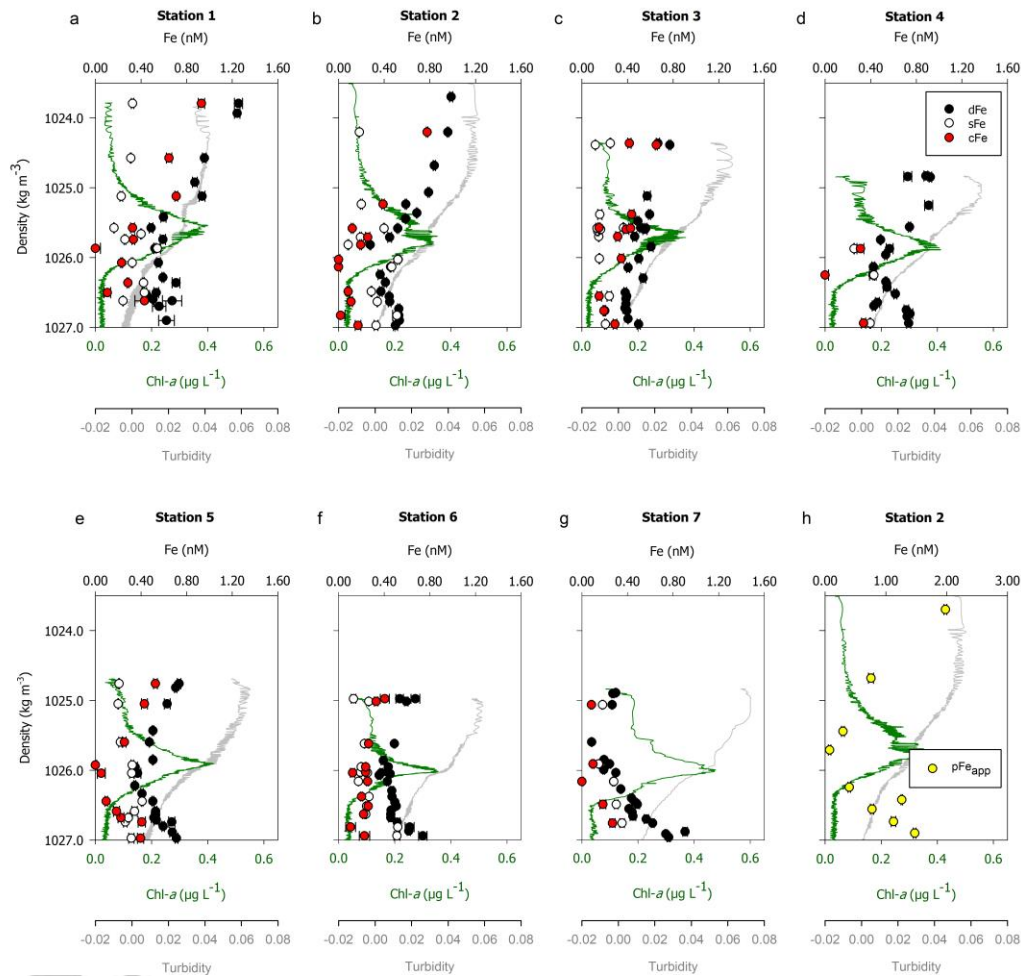
Figure 6 a-g) *Profiles of dFe (black), sFe (white) and cFe (red) against density in the upper water column at each station. **h)** Representative profile of pFe$_{app}$ (yellow) against density at Station 2. Error bars show one standard deviation of the mean concentration of three analytical replicates. For the calculated cFe and pFe$_{app}$ concentrations, associated measurement errors were propagated. Traces of Chl-a (green lines) and turbidity (grey lines, arbitrary units) are included.*
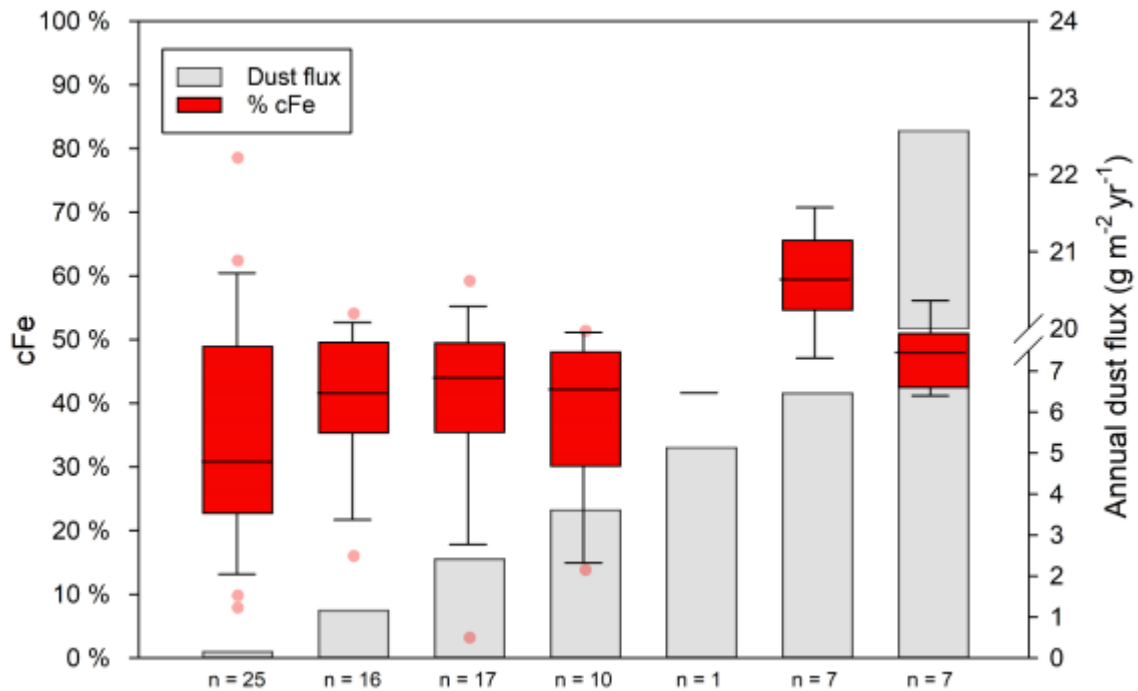
Figure 7 *Box plots of the partitioning of dFe into the colloidal fraction (red bars) at remineralisation depths of different oceanic regions, in order of increasing annual dust flux (grey) from left to right. Boxes represent the interquartile range, the middle line represents the median. Whiskers frame the 10th and 90th percentiles, while data points outside this range are shown as dots. The cFe data used in this plot were compiled from the present study and from Nishioka et al. (2001, 2013), Fitzsimmons, Carrasco, et al. (2015), Fitzsimmons, Hayes, et al. (2015), Bergquist et al. (2007), Ussher et al. (2010) and Chever et al. (2010), and binned by dust flux (see methods). Along the x-axis, n indicates the number of cFe measurements for each bin. For details on which data contributed to which bin the reader is referred to Table S1.*
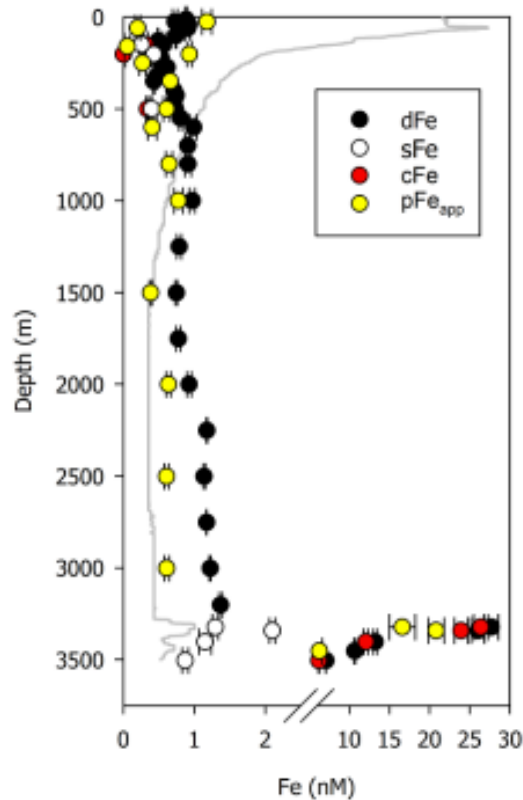
Figure 8 *Full-depth profile of dFe (black), sFe (white), cFe (red) and pFe_{app} (yellow) concentrations against depth at Station 4, located over the mid-Atlantic ridge. The turbidity trace (grey line) indicates the presence of the hydrothermal plume between 3300 m and 3500 m depth. Note the scale break for concentrations >2.5 nM. Error bars show one standard deviation of the mean concentration of three analytical replicates. For the calculated cFe and pFe_{app} concentrations, associated measurement errors were propagated.*
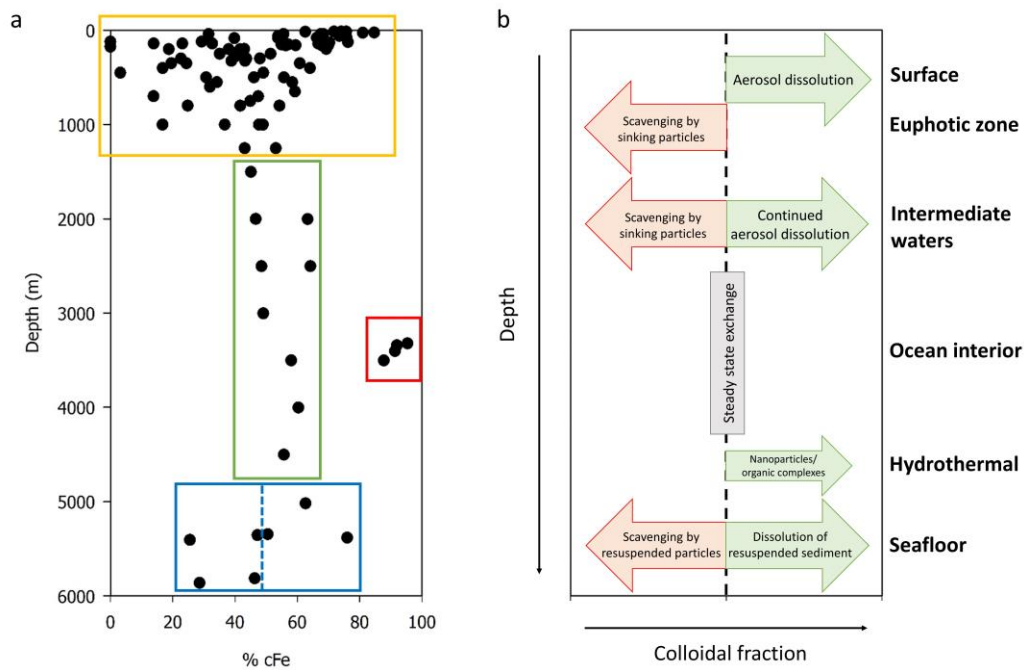
Figure 9 a) *The partitioning of dFe into the colloidal fraction against depth of the entire dataset, forming an hour glass-shape. The coloured boxes distinguish between the highly variable upper water column (yellow) and seafloor-water interface (blue, dotted blue line distinguishes between western and eastern basin), the narrow range of the deep ocean interior (green), and the hydrothermal signature (red).* ***b)*** *Conceptual model of the dominant processes throughout the water column, that drive the partitioning of the sFe and cFe away from the steady-state exchange of the ocean interior. Processes increasing and decreasing the colloidal fraction are highlighted in green and red, respectively.*